



Interface coupling induced built-in electric fields accelerate electro-assisted uranium extraction over $\text{Co}_3\text{O}_4/\text{FeO}_x$ nanosheet arrays

Li Zhou^{a,1}, Yi Li^{b,1}, Yuwen Shao^a, Jin Li^a, Gang Wu^a, Qiuyang Li^a, Xi Gong^a, Jie Lian^c, Xudong Cui^d, Wenkun Zhu^{a,*}, Tao Chen^{a,*}

^a State Key Laboratory of Environment-friendly Energy Materials, School of Environment and Resources, National Co-innovation Center for Nuclear Waste Disposal and Environmental Safety, Southwest University of Science and Technology, Mianyang 621010, PR China

^b School of Materials and Energy, University of Electronic Science and Technology, Chengdu 610000, PR China

^c CNNC Key Laboratory of Mass Spectrometry Analysis Technology, Chengdu 610000, PR China

^d Sichuan New Materials Research Center, Institute of Chemical Materials, China Academy of Engineering Physics, Chengdu 610200, PR China

ARTICLE INFO

Keywords:

$\text{Co}_3\text{O}_4/\text{FeO}_x$

Built-in electric field

M–O–H coordination bonds

Uranium extraction

ABSTRACT

Revealing the nature of enhanced electro-assisted uranium extraction activity by hetero-interface and M–O–H coordination bonds is an important and challenging task. Hence, $\text{Co}_3\text{O}_4/\text{FeO}_x$ nanosheet arrays with abundant M–O–H coordination bonds is fabricated as a binder-free and self-supporting electrocatalyst for electro-assisted uranium extraction from fluorine-containing uranium wastewater. As revealed by self-consistent energy band calculations and in-situ Kelvin Probe Force Microscopy (KPFM) analysis, the p–n heterojunction formed by $\text{Co}_3\text{O}_4/\text{FeO}_x$ provides a well-designed built-in electric field (BIEF), triggering the interfacial accumulation of uranium and accelerating the electro reduction kinetics of uranium. Consequently, $\text{Co}_3\text{O}_4/\text{FeO}_x$ shows remarkable U(VI) extraction ability (>95 %) in fluorine-containing uranium wastewater. By virtue of the XAFS spectra, free uranyl ions are captured by M–O–H on $\text{Co}_3\text{O}_4/\text{FeO}_x$ to form a sturdy $2\text{O}_{\text{ax}}-1\text{U}-3\text{O}_{\text{eq}}$ configuration, confirming the electrically driven separation of uranium and fluorine. Furthermore, DFT calculation indicates that the existent of M–O–H enhances the adsorption energy of uranium species, thus promoting uranium extraction efficiency.

1. Introduction

With the development and utilization of nuclear energy, the demand for uranium as the representative of nuclear fuel is increasing, resulting in a large number of uranium-containing radioactive wastewater [1–3]. As the most widespread existing uranium-containing radioactive wastewater, the fluorine-containing uranium wastewater with high fluorine concentration, high uranium content, large output, comes from uranium enrichment, uranium conversion, nuclear fuel element manufacturing and other processes [4–6]. The efficient enrichment and separation of uranium from radioactive fluorine wastewater holds significant importance in advancing nuclear environmental protection and promoting the sustainable development of nuclear energy.

Recently, electro-assisted reduction of soluble uranium (U(VI)) to neutral insoluble products is considered as an effective approach to realize uranium extraction [7–10]. For example, Tang et al.

demonstrated that modified molybdenum disulfide can be used as an electrocatalyst material in seawater to achieve high uranium extraction efficiency [11]. However, most reported traditional powder electrocatalysts required the introduction of polymer binders (such as nafion solutions) during the electrode preparation process, which inevitably increased the "dead volume" of the electrode materials [9,12]. Meanwhile, some inherent problems of binder-assisted electrocatalyst, such as the uncontrollability of microstructure, strong resistance to electrical conductivity, the coverage of active sites, etc., hinder the practical industrial application and are difficult to solve completely [13,14]. Therefore, developing a simple and general method to prepare binder-free and self-supporting electrocatalyst with controllable microstructure and composition for the treatment of fluorine-containing uranium wastewater is highly desirable.

Notably, the pivotal bottleneck for electro-assisted uranium extraction lies in the electrons transferred from the active center to the

* Corresponding authors.

E-mail addresses: zhuwenkun@swust.edu.cn (W. Zhu), chent@swust.edu.cn (T. Chen).

¹ These authors contributed equally to this work.

coordination site, which is closely related to excellent conductivity and abundant coordination sites for target electrocatalyst [15,16]. One helpful approach to adjust the conductivity of electrocatalyst is heterointerface engineering, considering that the introduction of heterogeneous catalysts will form a built-in electric field (BIEF) with interfacial bond chains between the original catalyst and heterogeneous catalyst [17,18]. Parallel to the heterointerface engineering, accelerating the confined capture and reduction of uranium usually comes from the tailored active sites though engineered the surface functional groups catalysts, which can be achieved easily by the introduction of metal-oxygen-hydrogen (M-O-H) coordination bonds [19]. Specifically, the construction of M-O-H (hard base) coordination bonds with specific recognition for uranyl ions (hard acid) based on the Hard-Soft-Acid-Base (HSAB) theory is expected to achieve efficient electro-assisted uranium extraction [20–22]. Therefore, the integration of heterointerface engineering and M-O-H coordination bonds provides a potential strategy to improve confined capture and reduction of uranium by engineering the electronic structure of binder-free and self-supporting electrocatalysts, and thereby enhancing the performance of electro-assisted uranium extraction.

Herein, we have successfully fabricated a powerful interface electric field in $\text{Co}_3\text{O}_4/\text{FeO}_x$ nanosheets arrays with abundant M-O-H coordination bonds to accelerate the confined capture and reduction of uranium species, resulting an accelerated uranium extraction kinetics in fluorine-containing uranium wastewater. By virtue of self-consistent energy band calculations and in-situ KPFM spectral analysis, we have proven the formation of well-designed BIEF between Co_3O_4 and FeO_x at the p-n heterojunction, offering a strong driving force and transportation highway for accelerating the charge directed migration. Accordingly, $\text{Co}_3\text{O}_4/\text{FeO}_x$ heterojunction exhibits superb uranium extraction capability, outstanding cyclic stability, and excellent selectivity performance for electrical reduction of uranium in fluorine-containing uranium wastewater. Trading on XAFS measurement, we confirm that the $\text{Co}_3\text{O}_4/\text{FeO}_x$ heterojunction with abundant M-O-H coordination bonds captured dissociate uranyl ions to form the sturdy $2\text{O}_{\text{ax}}-1\text{U}-3\text{O}_{\text{eq}}$ configuration, which can be achieved through electro-driven fluorine uranium separation. Theoretical calculations affirm that M-O-H coordination bonds in $\text{Co}_3\text{O}_4/\text{FeO}_x$ can enhance the affinity for uranium species, which has an important effect on the extraction capacity of uranium. The results provide a profound insight into the interface electric field for uranium extraction and a new avenue for screening the self-supporting electrocatalysts with considerable performances.

2. Experimental

2.1. Chemicals and materials

Fe foils were obtained from Alibaba. $\text{Co}(\text{NO}_3)_2 \cdot 6\text{H}_2\text{O}$ (AR, 99.0 %), $\text{UO}_2(\text{NO}_3)_2 \cdot 6\text{H}_2\text{O}$ (AR, 99.0 %), Na_2SO_4 (AR, 99.95 %), Na_2CO_3 (99.5 %), NaCl (AR, 99.5 %), $\text{Na}_2\text{C}_2\text{O}_4$ (AR, 99.5 %), NaNO_3 (AR, 99.0 %), and NaOH (AR, 95.0 %) were from Macklin Co., Ltd (Shanghai, China). CH_3COCH_3 (AR, 99.5 %) and $\text{CH}_3\text{CH}_2\text{OH}$ (AR, 99.7 %) were from ChengDu Chron Chemicals Co., Ltd.

2.2. Synthesis of FeO_x foils

The Fe foils ($2\text{ cm} \times 2\text{ cm}$) underwent a sequential washing process using CH_3COCH_3 , $\text{CH}_3\text{CH}_2\text{OH}$, and deionized water for 15 min each in an ultrasonic cleaning machine. After vacuum drying, the cleaned Fe foils were placed in the alumina boat and annealed at $500\text{ }^\circ\text{C}$ for 4 h ($2\text{ }^\circ\text{C min}^{-1}$) in air, to generate FeO_x foils.

2.3. Synthesis of $\text{Co}_3\text{O}_4/\text{FeO}_x$ nanosheet arrays

Firstly, FeO_x foils were placed in $\text{Co}(\text{NO}_3)_2 \cdot 6\text{H}_2\text{O}$ (0.1 M) aqueous solutions. After soaking for 12 h, the materials were dried at $120\text{ }^\circ\text{C}$ for

15 min. Next, the materials were annealed at $350\text{ }^\circ\text{C}$ for 30 min to accomplish the first load cycle (called $\text{Co}_3\text{O}_4/\text{FeO}_x-1$). The metal oxide nanosheet arrays on FeO_x foil were obtained by repeated loading cycles for several times (called $\text{Co}_3\text{O}_4/\text{FeO}_x-2$, $\text{Co}_3\text{O}_4/\text{FeO}_x-4$ and $\text{Co}_3\text{O}_4/\text{FeO}_x-6$).

2.4. Electrochemical measurements

The electrochemical measurements, such as cyclic voltammetry (CV) and electrochemical impedance spectroscopy (EIS), were conducted using the CHI 660E electrochemical workstation within a three-electrode system, in which $\text{Co}_3\text{O}_4/\text{FeO}_x$ was utilized as the working electrode, with Ag/AgCl serving as the reference electrode, Pt wire as the counter electrode, and 0.5 M Na_2SO_4 solutions acting as the electrolyte. And the voltage was set at -1.2 V . Electrocatalytic reduction of U(VI) was conducted by the single-chamber reactor (150 mL), and 50 mL fluorine-containing uranium solution (50 mg/L uranium and 1 g/L fluorine, unless otherwise specified) was put into the reactor. As for coexisting ion experiment, 500 mg/L of ion was added separately to the fluorine-containing uranium solution.

The following equation was used to compute removal ratio of uranium after electrocatalysis:

$$\text{Removal ratio} = (\text{C}_0 - \text{C}_t) / \text{C}_0 \times 100\%$$

Where C_0 is initial uranium concentration and C_t is uranium concentration after a certain amount of time has passed.

2.5. Characterizations

The morphologies of FeO_x and $\text{Co}_3\text{O}_4/\text{FeO}_x$ were examined using Scanning Electron Microscopy (SEM, ZEISS Gemini 300) and Transmission Electron Microscopy (TEM, FEI TF2). The structure of the materials was conducted on High Resolution Transmission Electron Microscope (HRTEM, FEI TF2s), X-ray Diffraction Patterns (XRD, Rigaku Ultima IV) and Raman Spectroscopy (HORIBA Scientific LabRAM HR Evolution). The electronic structure of the materials was performed through Ultraviolet-Visible Diffuse Reflectance Spectra (UV-vis, UV-3600i Plus). The concentration of uranium was measured through Inductively Coupled Plasma-Optical Emission Spectrometer (ICP-OES, Agilent 5110) and Inductively Coupled Plasma Mass Spectrometry (ICP-MS, Agilent 7800). The oxygen vacancy of the materials was recorded by Electron Spin Resonance (ESR, A300-10/12 instrument, Germany Bruker). The functional groups were acquired the Fourier Transform Infrared Spectroscopy (FT-IR, Spectrum One Autoima). The water contact angles were measured using Dataphysics OCA20. Ultraviolet Photoelectron Spectroscopy (UPS) characterizations were measured on Thermo ESCALAB 250XI. The valence of Fe, Co, O and uranium was measured by X-ray Photoelectron Spectroscopy (XPS, Thermo Scientific K-Alpha). The uranium structure was performed with X-ray Absorption Fine Structure Spectroscopy (XAFS, Beijing Synchrotron Radiation Factory). The surface potential of the materials was conducted using Kelvin Probe Force Microscopy (KPFM, Bruker Dimension Icon).

3. Results and discussions

3.1. Preparation and structure of $\text{Co}_3\text{O}_4/\text{FeO}_x$

As illustrated in Fig. 1a, $\text{Co}_3\text{O}_4/\text{FeO}_x$ nanosheet arrays were obtained by the continuous two-step heat treatment strategies. To begin with, FeO_x nanosheet arrays were prepared by annealing at $500\text{ }^\circ\text{C}$ for 4 h. And then, the FeO_x nanosheet arrays were immersed in the $\text{Co}(\text{NO}_3)_2 \cdot 6\text{H}_2\text{O}$ aqueous solution as the precursor for 12 h. After drying, the $\text{Co}_3\text{O}_4/\text{FeO}_x$ nanosheet arrays were obtained by annealing in air. As illustrated in the top-view SEM image (Fig. 1b), the metal oxide nanosheets with an average thickness of 20 nm were uniformly and vertically

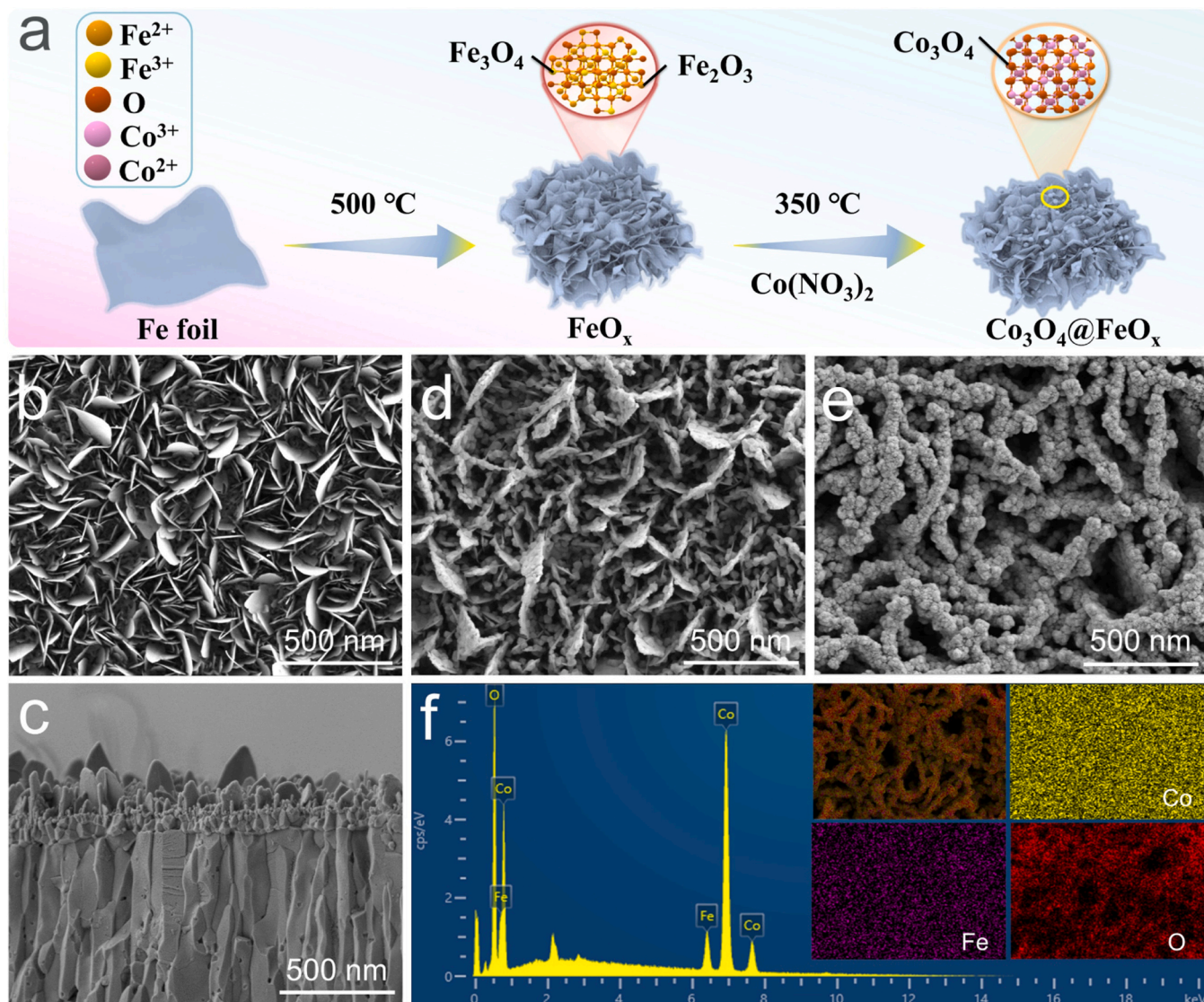


Fig. 1. (a) Schematic diagram of $\text{Co}_3\text{O}_4@\text{FeO}_x$ preparation; (b) The top-view SEM image of FeO_x ; (c) The side-view SEM image of FeO_x ; (d, e) The top-view SEM image of $\text{Co}_3\text{O}_4@\text{FeO}_x$ -1 and $\text{Co}_3\text{O}_4@\text{FeO}_x$ -4, respectively; (f) EDS spectra and elemental mappings of $\text{Co}_3\text{O}_4@\text{FeO}_x$ -4.

arranged on the surface of Fe foil after high-temperature annealing. In addition, the side-view SEM image displayed a distinct layered structure of nanosheets, which may be assigned to the heterogeneous interface between Fe-based oxides and Fe foils (Fig. 1c). After being soaked in cobalt nitrate and annealed for the first cycle, we can observe that Co_3O_4 nanoparticles were uniformly loaded on the FeO_x nanoarrays surface (Fig. 1d, Fig. S1a). With the increase of the amount of Co, the FeO_x nanosheets arrays had been completely covered by the annealed Co_3O_4 nanoparticles (Fig. 1e, Fig. S1b). The energy dispersive spectrometer (EDS) showed the presence of Co, Fe, and O peaks (Fig. 1f). Meanwhile, the elemental mapping indicated the Co, Fe, O were dispersed in the $\text{Co}_3\text{O}_4@\text{FeO}_x$ -4. In addition, high-temperature annealing did not damage the whole structure of Fe foil, and a uniformly distributed nanosheets arrays was formed on its surface in situ, which can be confirmed by optical photos of the Fe foil, FeO_x and $\text{Co}_3\text{O}_4@\text{FeO}_x$ (Fig. S2). The above results showed that $\text{Co}_3\text{O}_4@\text{FeO}_x$ nanosheet arrays can be obtained easily by thermal decomposition of $\text{Co}(\text{NO}_3)_3$ deposited on FeO_x .

In addition, the morphologies and crystal structures of the well-prepared FeO_x and $\text{Co}_3\text{O}_4@\text{FeO}_x$ were recorded on TEM. As for FeO_x , the standard two-dimensional thin nanosheets are exhibited in Fig. 2a. The HRTEM image of FeO_x showed that significant interplanar spacing of 0.368 nm and 0.242 nm were corresponded to (012) plane of Fe_2O_3

and (222) plane of Fe_3O_4 , respectively (Fig. 2b). With the introduction of Co_3O_4 , a large number of nanoparticles were uniformly loaded on the nanosheets (Fig. S3). And the HRTEM image of $\text{Co}_3\text{O}_4@\text{FeO}_x$ in Fig. 2c showed two obviously different lattice stripes with lattice spacing of 0.296 nm and 0.243 nm, respectively, which corresponded to the (220) crystal plane of Fe_3O_4 and (311) crystal plane of Co_3O_4 . The distinct heterojunction was noticed between FeO_x and Co_3O_4 , which was favorable for electron transfer. As depicted in Fig. S4 and S5, the elemental mappings exhibited that Fe and O were dispersed uniformly in the FeO_x nanosheet and Co was scattered on the $\text{Co}_3\text{O}_4@\text{FeO}_x$, in consistent with SEM-EDS mapping.

In order to examine the crystal structure, Fe foil, FeO_x , $\text{Co}_3\text{O}_4@\text{FeO}_x$ are subjected to XRD patterns. The characteristic peaks at 44.6°, 65.0°, and 82.3° corresponded to the Fe foil, respectively (PDF#06-0696) (Fig. S6a). The characteristic peaks of FeO_x at 24.1°, 33.2°, 35.6°, 40.9°, 62.4° were the Fe_2O_3 , respectively (PDF#33-0664). And the characteristic peaks at 30.0°, 35.4°, 43.0°, 53.4°, 56.9°, 62.5° were the Fe_3O_4 , respectively (PDF#99-0073, Fig. S6b). As for $\text{Co}_3\text{O}_4@\text{FeO}_x$, we can observe that the characteristic peaks at 19.0°, 31.3°, 36.8°, 44.8°, 59.3°, and 65.2° corresponded to the (111), (220), (311), (400), (511), and (440) crystal planes of Co_3O_4 , respectively (PDF#74-2120) (Fig. S6c, Fig. 2d). More importantly, the crystallinity and structural integrity of

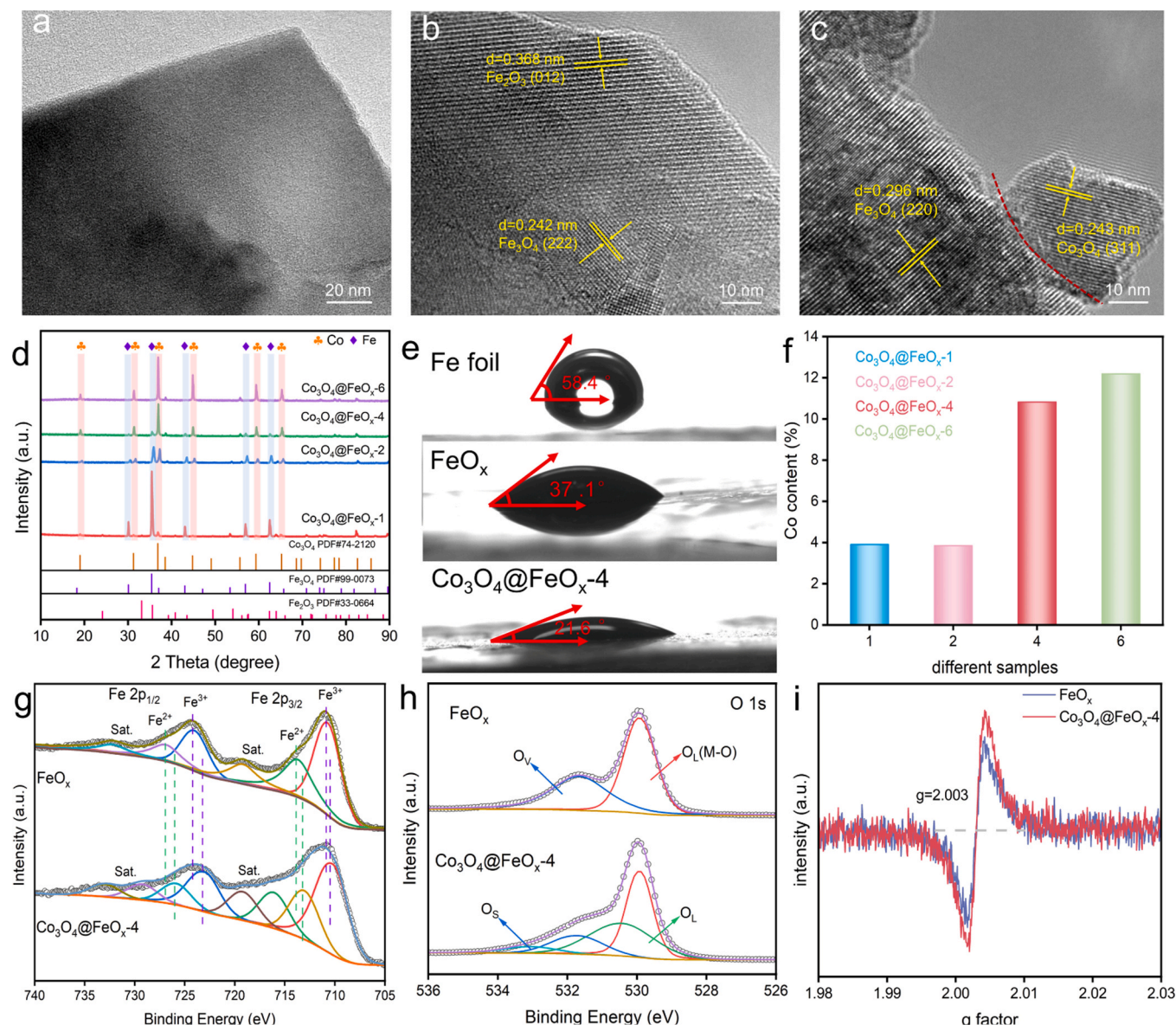


Fig. 2. (a) TEM image of FeO_x; (b) HRTEM image of FeO_x; (c) HRTEM image of Co₃O₄@FeO_x-4; (d) XRD patterns of Co₃O₄@FeO_x; (e) The contact angles of Fe foil, FeO_x, Co₃O₄@FeO_x-4; (f) The content of Co for different samples; (g) Fe 2p XPS spectra of FeO_x and Co₃O₄@FeO_x-4; (h) O 1s XPS spectra of FeO_x and Co₃O₄@FeO_x-4; (i) ESR spectra of FeO_x and Co₃O₄@FeO_x-4.

Fe₂O₃, Fe₃O₄ and Co₃O₄ were well maintained after thermal decomposition of Co₃O₄@FeO_x. Accordingly, the structure of FeO_x and Co₃O₄@FeO_x were further confirmed by the Raman spectra (Fig. S7). Five strong peaks of FeO_x at 222.4, 288.9, 406.8, 494.9, and 606.6 cm⁻¹ were corresponding to the A₁g and E_g [23]. As for Co₃O₄@FeO_x, the peaks about 193.2, 480.9, 521.2 and 689.4 cm⁻¹ were static to the F₂g, E_g, F₂g, and A₁g phonon modes of crystalline Co₃O₄ [24–26].

To verify the influence of heat treatment on the surface hydrophobicity of materials, we further conducted water contact angle measurements [21]. The contact angle of Fe foil was 58.4°, whereas for FeO_x, the water contact angle was 37.1°. After surface thermal deposition, the water contact angle of Co₃O₄@FeO_x was much lower at 21.6° (Fig. 2e). The results showed that Co₃O₄ nanoparticles loaded on the surface of FeO_x greatly enhanced the hydrophilicity of the materials, which were expected to provide an abundance of active sites for the uranium adsorption in fluorine-containing uranium wastewater.

To further confirm the presence of M-O-H in the Co₃O₄@FeO_x nanosheet arrays, we conducted the XPS, ESR and FT-IR measurements. As illustrated in Fig. S8, the XPS of Co₃O₄@FeO_x clearly showed three

peaks corresponding to Co, Fe, O. Meanwhile, the samples (Co₃O₄@FeO_x-1, Co₃O₄@FeO_x-2, Co₃O₄@FeO_x-4, and Co₃O₄@FeO_x-6) with different loading cycles were tested by ICP. As depicted in Fig. 2f, the difference between the Co content of the first cycle and the two cycles was not much, about 3.9 %. Compared with the Co₃O₄@FeO_x-4 and Co₃O₄@FeO_x-6, the Co content increased and reached more than 10 %. Besides, the peak intensities of Co strengthen, indicating that the surface was covered with an excess of Co₃O₄. As illustrated in the Fe 2p spectra of FeO_x (Fig. 2g), the main peaks were divided assigning to Fe³⁺ at 726.8 eV and 713.9 eV, and Fe²⁺ at 724.2 eV and 710.8 eV, respectively. The adhesion of Co₃O₄ on the surface of FeO_x led to the change of the microchemical environment of the composite. The charge state of Fe changed and caused a shift in binding energy towards the low-energy region, resulting from the electron transfer between FeO_x and Co₃O₄ [27,28]. As depicted in Fig. S9, the high resolution of Co 2p was analyzed, revealing two distinct sets of peaks, where the peaks at 795.8 eV and 780.6 eV corresponded to 2p_{1/2} and 2p_{3/2} of Co²⁺, while the peaks at 794.2 eV and 779.3 eV corresponded to 2p_{1/2} and 2p_{3/2} of Co³⁺, which further confirmed the successful synthesis of Co₃O₄ [29]. As

seen in Fig. 2h, the O 1s spectrum was analyzed, and three primary peaks were observed at 529.9 eV, 531.6 eV, and 533.1 eV, which can be attributed to different oxygen species. Specifically, the peak at 529.9 eV corresponded to lattice oxygen (O_L), the peak at 531.6 eV corresponded to surface active oxygen vacancies (O_V), and the peak at 533.1 eV corresponded to surface adsorbed oxygen (O_S) [30,31]. Due to the in-situ formation of Co_3O_4 , a lot of crystallographic defects appeared on the FeO_x surface, which made the unsaturated coordination in FeO_x was more likely to form M-O-H coordination bonds [29]. In addition, the ESR results can further confirm that $Co_3O_4@FeO_x$ the surface contained a large number of lattice defects [32]. As illustrated in Fig. 2i, the ESR spectrum of $Co_3O_4@FeO_x$ presented a significantly a strong signal at $g=2.003$, further verifying the existence of abundant oxygen vacancy defects in the $Co_3O_4@FeO_x$. Furthermore, the FT-IR spectra of FeO_x and $Co_3O_4@FeO_x-4$ were measured (Fig. S10). Compared to the FT-IR of FeO_x , a new prominent broad peak at 3251.39 cm^{-1} was observed in the $Co_3O_4@FeO_x-4$, which was attributed to the stretching vibration of hydroxyl groups, indicating the presence of -OH.

The above results suggested that in-situ loading of Co_3O_4 on the surface of FeO_x induced the formation of a lot of M-O-H, which was beneficial for improving the selective capture of uranium.

3.2. Electrochemical performance for uranium extraction

The M-O-H-enriched $Co_3O_4@FeO_x$ offered a promising foundation for electro-assisted uranium extraction from fluorine-containing uranium wastewater. The three-electrode system was conducted to consider the electro-assisted uranium extraction performance of $Co_3O_4@FeO_x$. First of all, we studied the uranium removal performance of different samples (Fig. 3a). The pristine FeO_x exhibited a relatively lower removal ability for U(VI) was 79.05 %. With the introduction of Co_3O_4 , the U(VI)

extraction efficiency in fluorine-containing uranium wastewater of $Co_3O_4@FeO_x$ was 97.12 %, 97.95 %, and 97.68 %, respectively. In addition, we considered the influence of different annealing temperatures on the electrode materials. The results showed that the removal of uranium by $Co_3O_4@FeO_x-4$ (annealing temperature: 500 °C) was the excellent in the fluorine-containing uranium wastewater (Fig. S11). The increased U(VI) extraction capacity was ascribed to enriched active sites derived from the nanosheet array structure and the faster charge transfer rate between Co_3O_4 and FeO_x .

Taking the $Co_3O_4@FeO_x-4$ as an example, we also assessed the influence of the pH, reaction time, initial uranium concentration, and different voltage on the U(VI) extraction in the simulated fluorine-containing uranium wastewater. As for $Co_3O_4@FeO_x-4$, when the pH was 3, the increased concentration of hydrogen ions accelerated the hydrogen evolution reaction, causing interference with the electrochemical reduction of uranium. As the pH increased, the removal capacity exhibited a continuous upward trend and reached maximum value at pH 5–6. When the pH exceeded 6, there was a decrease in the removal capacity (Fig. 3b). The above results can be ascribed to the pH-dependent speciation of uranium species. In order to explain the above point, the uranium species in simulated wastewater at various pH was modeled. As displayed in Fig. S12, within the pH range of 2–6, uranium species remained comparatively sensitive to change in pH, where the prevailing uranium species were $UO_2F_2(aq)$, UO_2F_3 and $UO_2F_4^{2-}$, while a small fraction of uranium was present as UO_2F^+ . Between the pH 6–10, the uranium species of UO_2F_3 and $UO_2F_4^{2-}$ undergone significant changed with the increasing pH, and the uranium specie was largely in the form of $UO_2(CO_3)_3^{4-}$. Thus, at elevated pH levels, the uranium extraction rate decreased due to the electrostatic repulsion between the cathode and the negatively charged uranium species. This repulsion slowed down the migration of uranium species towards the $Co_3O_4@FeO_x-4$ electrodes,

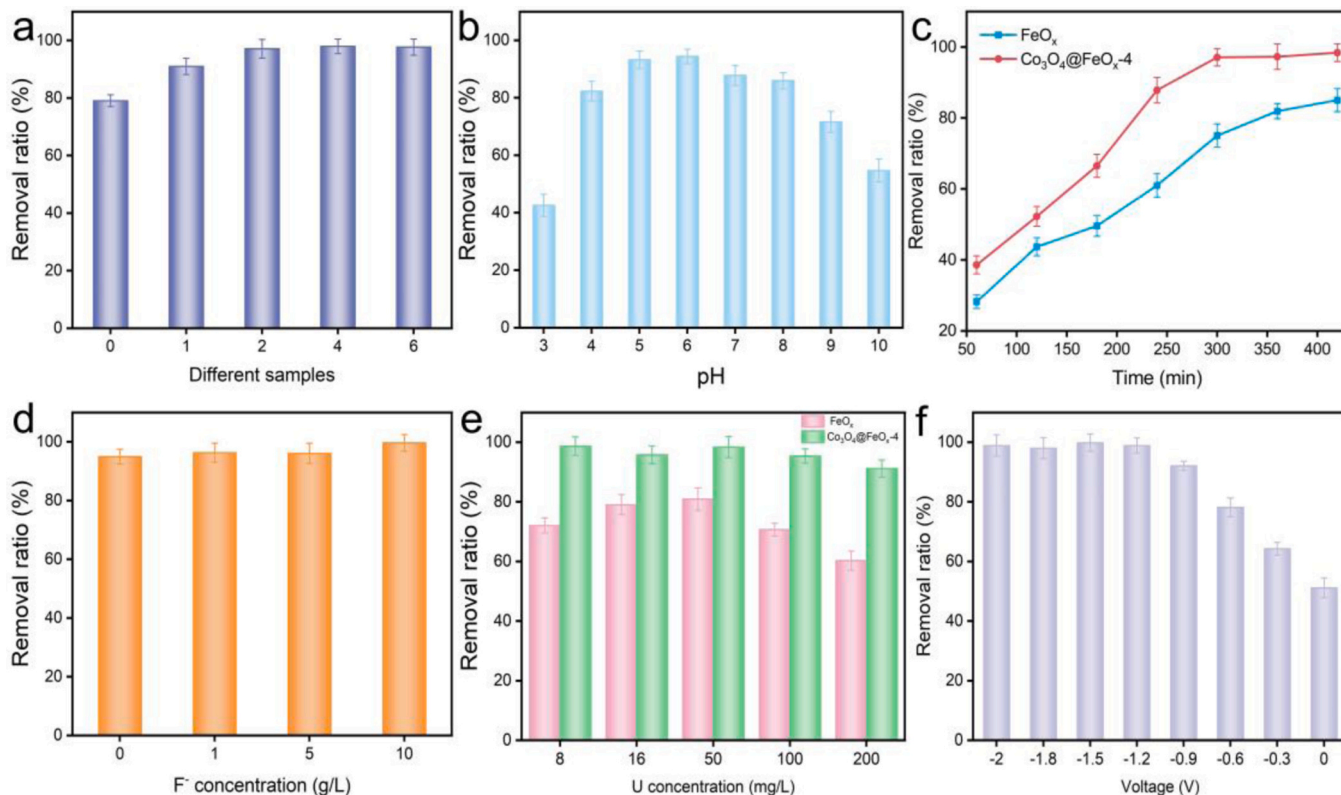


Fig. 3. (a) The removal ratios of U(VI) via different samples, such as FeO_x , $Co_3O_4@FeO_x-1$, $Co_3O_4@FeO_x-2$, $Co_3O_4@FeO_x-4$, $Co_3O_4@FeO_x-6$ (U(VI): 50 mg/L, F: 1 g/L); (b) The removal efficiency of $Co_3O_4@FeO_x-4$ at different pH (U(VI): 50 mg/L, F: 1 g/L); (c) The removal effect of U(VI) by $Co_3O_4@FeO_x-4$ in different time (U(VI): 50 mg/L, F: 1 g/L); (d) The effect of different F^- concentrations on U(VI) removal ratio (U(VI): 50 mg/L); (e) The influence of U(VI) concentrations on removal ratio (F: 1 g/L); (f) The effect of different voltage on U(VI) removal ratio (U(VI): 50 mg/L, F: 1 g/L).

leading to a reduced rate of uranium extraction.

Under the action of an applied electric field, the U(VI) extraction efficiency of FeO_x reached 60.98 %, 75.04 % within 240 min and 300 min in the existence of F^- , respectively. After introduction of Co_3O_4 , the U(VI) extraction capacity of $\text{Co}_3\text{O}_4/\text{FeO}_x$ -4 was 87.82 %, 97.08 % under the same reaction conditions within 240 min and 300 min, respectively (Fig. 3c). The effect of different F^- on uranium removal was also studied. In the case of 10 g/L F^- , we can observe that the extraction efficiency of $\text{Co}_3\text{O}_4/\text{FeO}_x$ -4 for U(VI) was 99.61 % (Fig. 3d). All of these results proved that $\text{Co}_3\text{O}_4/\text{FeO}_x$ -4 indicated the high extraction efficiency of uranium in the high fluorine-containing uranium wastewater.

The impact of uranium concentration was assessed using a range of initial uranium concentrations spanning from 8 mg/L to 200 mg/L. The range covered the uranium concentrations frequently reported in different uranium wastewater. As exhibited in Fig. 3e, the U(VI) extraction capacity of $\text{Co}_3\text{O}_4/\text{FeO}_x$ -4 at the fluorine-containing wastewater of uranium concentrations ranging from 8 mg/L to 200 mg/L maintained at an average of 96 %, indicating that the impact of uranium concentration within the 8–200 mg/L range on the electrochemical uranium extraction process was negligible. In addition, considering the importance of the irradiation stability of electrode materials in the treatment of real uranium-containing radioactive wastewater, we evaluated the capacity of $\text{Co}_3\text{O}_4/\text{FeO}_x$ -4 treated with ^{60}Co γ -ray irradiation in the range of 10–200 kGy in removing uranium from fluorine-containing uranium wastewater. As shown in Fig. S13a, after being irradiated with doses ranging from 10 kGy to 200 kGy, the removal efficiency of U(VI) by $\text{Co}_3\text{O}_4/\text{FeO}_x$ -4 did not significantly decrease. In addition, the SEM and phase structure showed that $\text{Co}_3\text{O}_4/\text{FeO}_x$ -4 was hardly affected by irradiation, which indicated that $\text{Co}_3\text{O}_4/\text{FeO}_x$ -4 possessed high irradiation stability (Fig. S13b, c).

The operating conditions of electrochemical workstation directly influence the efficiency of uranium reduction. The applied electric field can promote the migration of dissolved uranium to $\text{Co}_3\text{O}_4/\text{FeO}_x$ -4. Thus, we further investigated the voltage from -2.0 – 0 V to check the U(VI) removal ability in the fluorine-containing uranium wastewater

(Fig. 3f). With the increase of voltage absolute value, the electric field force enhanced, resulting the rate of negative electrode adsorbing U(VI) increased. $\text{Co}_3\text{O}_4/\text{FeO}_x$ -4 showed the highest U(VI) removal efficiency (> 95 %) at low voltage of -1.2 V. Additionally, the removal ability at 0 V for $\text{Co}_3\text{O}_4/\text{FeO}_x$ -4 was 51.10 %, indicating the presence of physico-chemical adsorption. The above results indicated that the $\text{Co}_3\text{O}_4/\text{FeO}_x$ -4 had great potential for energy conserving during U(VI) removal.

The unique nanosheet arrays in $\text{Co}_3\text{O}_4/\text{FeO}_x$ encourage us to investigate the electrochemical extraction of uranium in fluorine-containing uranium wastewater through the three-electrode system. At first, we investigate CV curves at different scan rates (Fig. S14). Within the voltage range spanning from 0 V to -1.0 V (vs Ag/AgCl), clear reduction peaks were observed in the region of -0.8 V to -1.0 V, further confirming the uranium species were confined and reduced by $\text{Co}_3\text{O}_4/\text{FeO}_x$. In addition, EIS was employed to examine the electrochemical properties of FeO_x and $\text{Co}_3\text{O}_4/\text{FeO}_x$ -4 (Fig. S15). The Equivalent series resistance (R_s) was a combination of the electrolyte ion resistance and the electrode material resistance. The R_s of FeO_x and $\text{Co}_3\text{O}_4/\text{FeO}_x$ -4 were only a few differences. The Nyquist curve of FeO_x and $\text{Co}_3\text{O}_4/\text{FeO}_x$ -4 consisted of a high frequency arc and a low frequency diagonal. The results indicated that the low-frequency linear portion of $\text{Co}_3\text{O}_4/\text{FeO}_x$ -4 was steeper than that of FeO_x , suggesting that the ion diffusion coefficient of $\text{Co}_3\text{O}_4/\text{FeO}_x$ -4 electrode was higher than that of FeO_x [15].

Subsequently, we studied the reusability of $\text{Co}_3\text{O}_4/\text{FeO}_x$ -4 via repetitive uranium electro-reduction cycles in fluorine-containing uranium wastewater (Fig. 4a). Specifically, $\text{Co}_3\text{O}_4/\text{FeO}_x$ -4 still retained a rather high removal capacity for uranium after ten cycles, further confirming the excellent cycling stability and practicality of the integrated electrode. Considering that a great amount of interference ions in the nuclear fuel cycle process would affect the uranium extraction, the resistance to interference and selectivity of $\text{Co}_3\text{O}_4/\text{FeO}_x$ -4 in fluorine-containing uranium wastewater were further calculated. At first, we tested the competitive adsorption performance of the electrode material. $\text{Co}_3\text{O}_4/\text{FeO}_x$ -4 exhibited poor uranium adsorption performance and

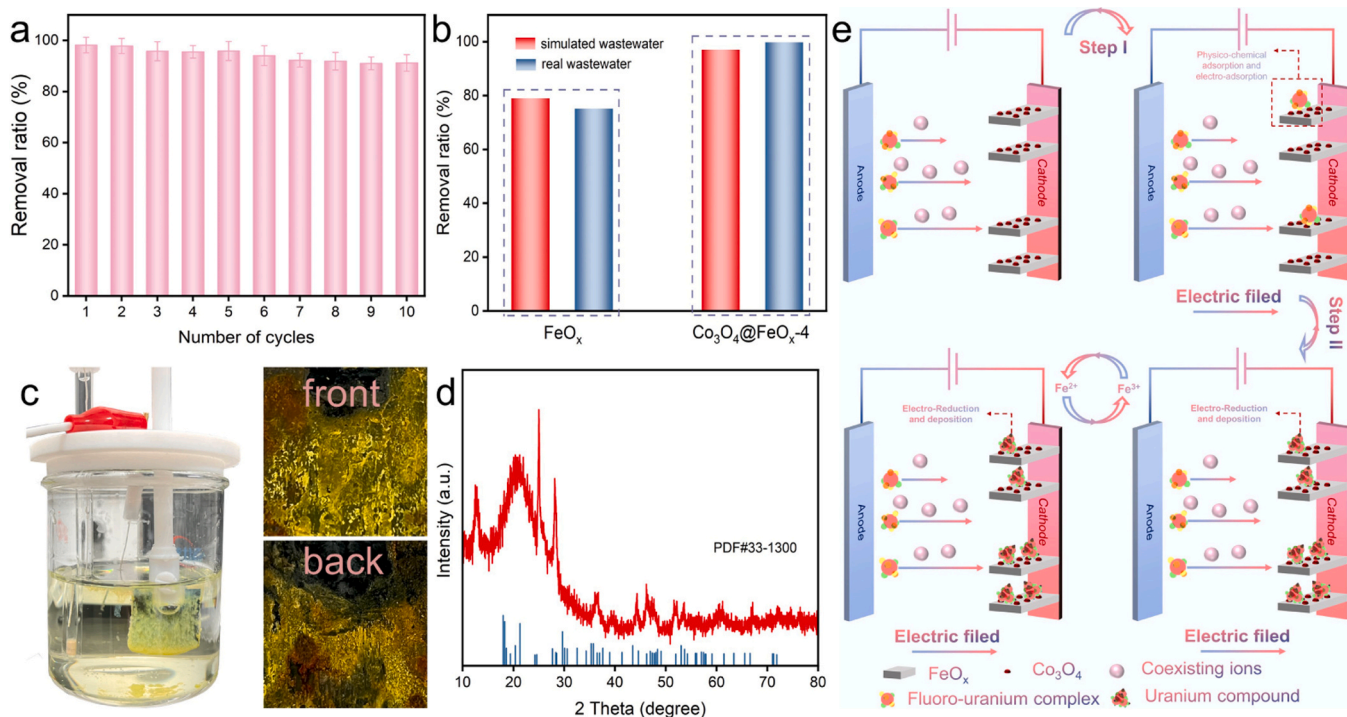


Fig. 4. (a) The reuseability of $\text{Co}_3\text{O}_4/\text{FeO}_x$ -4 for uranium removal (U(VI): 50 mg/L, F^- : 1 g/L); (b) The removal efficiency of $\text{Co}_3\text{O}_4/\text{FeO}_x$ -4 at simulated fluorine-containing uranium wastewater and real uranium-containing wastewater; (c) The photograph of three-electrode system in reaction (left) and the photograph of $\text{Co}_3\text{O}_4/\text{FeO}_x$ -4 electrode (right), (U(VI): 1000 mg/L, F^- : 1 g/L); (d) The corresponding XRD pattern; (e) The mechanism of uranium extraction for $\text{Co}_3\text{O}_4/\text{FeO}_x$.

lacked selectivity (Fig. S16a, b). Compared to traditional adsorption, the ability of electro-assisted uranium extraction can still reach over 85 % in the presence of a large number of interfering ions (Fig. S16c, d). Notably, the presence of Fe^{3+} redox ions in the solution led to a slight decrease in the removal efficiency of U(VI), which was attributed to the substantial consumption of electrons during the oxidation-reduction process of Fe^{3+} . The results indicated that electrochemical method had more potential and effectiveness compared to adsorption method in treating fluorine-containing uranium wastewater. Based on the data from above experiments, the electrochemical removal efficiency of real industrial uranium-containing wastewater was further evaluated using $\text{Co}_3\text{O}_4/\text{FeO}_x$ -4. Even in the presence of high concentrations of anions (Tab. S1), the removal efficiency of $\text{Co}_3\text{O}_4/\text{FeO}_x$ -4 exceeded 99.8 % (Fig. 4b). This was because the interfacial reactions of $\text{Co}_3\text{O}_4/\text{FeO}_x$ contributed to improving the extraction efficiency and selectivity. The results demonstrated that $\text{Co}_3\text{O}_4/\text{FeO}_x$ is a promising electrode material for treatment of industrial uranium-containing wastewater. Furthermore, compared to existing electrocatalysts, $\text{Co}_3\text{O}_4/\text{FeO}_x$ exhibited excellent uranium removal capacity (Tab. S2). Given the analysis, we consider $\text{Co}_3\text{O}_4/\text{FeO}_x$ to be a promising candidate material for U (VI) removal.

To further visually observe the reduction deposition process of uranium species on the electrode surface, we conducted electrochemical extraction experiments under high concentration of uranium. As shown in the Fig. 4c, after a period of time, we observed that pale-yellow floc produced around the $\text{Co}_3\text{O}_4/\text{FeO}_x$ -4. With the increase of time, the darker yellow product formed was pushed away from the $\text{Co}_3\text{O}_4/\text{FeO}_x$ -4 surface by bubbles and precipitated to the bottom of the electrolysis cell. Due to the action of bubbles, most of the electrodeposited precipitate settled to the bottom of the electrolysis cell and a small amount remained on the $\text{Co}_3\text{O}_4/\text{FeO}_x$ -4. Accordingly, uranium precipitates can be collected by filtration only from the solution in the study (Fig. S17). And uranium precipitates (284 mg) consumed electricity 309.24 mW h in the fluorine-containing uranium wastewater (Fig. S18). Furthermore, the reacted precipitate was tested by XRD to verify the crystal structure of the uranium species after reaction (Fig. 4d). The XRD spectrum of reacted precipitate displayed several peaks at 20.2° , 28.3° , 36.4° , and 46.2° of $\text{Na}_2\text{UO}_2\text{F}_6$ (PDF#33-1300), respectively, further confirming the capture and reduction process of highly valent uranium species. Moreover, we utilized the XPS characterization to verify the change the surface chemical change in the reaction. For the high-resolution Fe 2p XPS spectra, as the uranium extraction process unfolded, the Fe 2p peaks of $\text{Co}_3\text{O}_4/\text{FeO}_x$ -4 shifted to higher binding energy and the $\text{Fe}^{2+}/\text{Fe}^{3+}$ ratio decreased at first and then increased (Fig. 2g and Fig. S19), which showed that there was a good redox cycle of $\text{Fe}^{2+}/\text{Fe}^{3+}$ inside, thus guaranteeing the reduction of uranium [33,34].

3.3. Electrochemical mechanism

In order to verify the U-F separation process, DFT calculations were employed to analyze the reaction pathway. The optimized model of the crucial species during the UO_2F^+ adsorption and dissociation process is depicted in Fig. S20. The bond length between F and U in the free UO_2F^+ was determined to be 2.09 Å. Upon approaching the surface, UO_2F^+ engaged in interactions with the surface O atoms, where U-F bond length underwent very little change. This adsorption process involved the transfer of charge between UO_2F^+ and the material. Under the action of Coulomb force, the U-F bond in UO_2F^+ was broken, resulting in the separation of UO_2^+ and F^- as a transition state, necessitating an activation energy of 0.75 eV for the process. During the transition state, the F-U bond was cleaved, leading to energy redistribution and facilitating a reduction reaction. Building upon the above analysis, the mechanism of $\text{Co}_3\text{O}_4/\text{FeO}_x$ electrodes for uranium extraction from fluorine-containing uranium wastewater was developed (Fig. 4e). First of all, physico-chemical adsorption and electro-adsorption of fluoro-uranium complex by M-OH groups of $\text{Co}_3\text{O}_4/\text{FeO}_x$ fast transferred onto the surface of electrodes under the electric field. Subsequently, the F-U bond

in the electro-assisted fluoro-uranium complex was broken and further electro-reduction to the neutral uranium compounds and deposited on the electrode surface. Due to the coexistence of Fe^{2+} and Fe^{3+} in $\text{Co}_3\text{O}_4/\text{FeO}_x$ and the release of the active center, an increasing quantity of fluoro-uranium complexes was electrostatically adsorbed and subsequently subjected to electro-reduction/deposition on the electrode surface, which endowed excellent adsorption capacity and selectivity.

To gain deeper insights into the influence mechanism of interface electric field enhancement on the electro-assisted uranium extraction, we used self-consistent energy band calculation and DFT calculation. At first, UV-vis spectroscopy was employed to investigate the band gaps of Co_3O_4 , FeO_x , and $\text{Co}_3\text{O}_4/\text{FeO}_x$. As illustrated in Fig. S21, the bandgap energies (E_g) of Co_3O_4 , FeO_x , and $\text{Co}_3\text{O}_4/\text{FeO}_x$ were calculated as 2.30 eV, 2.41 eV, and 2.19 eV by Kubelka-Munk method, respectively [35,36]. The bandgap of $\text{Co}_3\text{O}_4/\text{FeO}_x$ was smaller than those of Co_3O_4 and FeO_x , which meant the faster electron transfer and facilitated catalytic reaction. The Mott-Schottky (MS) curves suggested that Co_3O_4 exhibited p-type semiconductor characteristics with a negative slope, and FeO_x showed n-type semiconductor traits with a positive slope (Fig. S22) [37]. By intersecting the tangent line of the slope with the horizontal coordinate, the flat band potentials of Co_3O_4 and FeO_x were determined to be 0.81 V and -0.96 V, respectively. In addition, the MS of $\text{Co}_3\text{O}_4/\text{FeO}_x$ -4 showed the conspicuous "V-shape", suggesting the construction of a typical p-n heterojunction between Co_3O_4 and FeO_x (Fig. S23) [38].

The electron transfer characteristics between Co_3O_4 and FeO_x are intricately connected to the work function difference ($\Delta\Phi$) in p-n heterojunction. UPS spectroscopy was employed to calculate work functions (Φ) values of Co_3O_4 and FeO_x . As depicted in Fig. 5a and b, the Φ values of Co_3O_4 and FeO_x were calculated to be 4.95 eV and 5.65 eV based on the following equation: $\Phi = h\nu + E_{\text{cutoff}} - E_{\text{Fermi}}$, respectively, revealing a relatively substantial $\Delta\Phi$ of 0.7 eV at the $\text{Co}_3\text{O}_4/\text{FeO}_x$ interface. Co_3O_4 exhibited a lower work function in comparison to FeO_x , indicating the potential for electron transfer from Co_3O_4 to FeO_x . As shown in Fig. S24, the valence bands of Co_3O_4 and FeO_x were 0.50 eV and 1.20 eV, respectively. Thus, the positions of valence band (E_{VB}) for Co_3O_4 and FeO_x were equal to 0.95 eV and 2.35 eV vs. NHE, respectively. As a result, the respective positions of the conduction band (E_{CB}) were calculated to be 1.35 eV and -0.06 eV, respectively (based on $E_g = E_{\text{VB}} - E_{\text{CB}}$) [39].

Furthermore, we employed DFT calculation to verify the electron transfer between Co_3O_4 and Fe_3O_4 . The optimized model for the $\text{Co}_3\text{O}_4/\text{FeO}_x$ heterojunction involved selecting the Co_3O_4 (220) and Fe_3O_4 (311) surfaces. Upon contact between Co_3O_4 and Fe_3O_4 , the Co and Fe engaged in the formation of Co-O-Fe bonds coordination bond. The Co-O-Fe coordination bond stabilized the material structure and hindered the migration of oxygen atoms, resulting in enhanced material stability and increased efficiency in oxidation-reduction reactions (Fig. S25). In addition, the electron transfer characteristics in the p-n heterojunction were elucidated through the calculation of charge density differences (Fig. 5c), where the yellow and cyan regions denote the areas of electron accumulation and electron depletion, respectively. Obviously, the interaction of between Co_3O_4 and Fe_3O_4 led to localized charge redistribution at the atomic interface, initiating electron migration from Co_3O_4 to Fe_3O_4 . The calculated Φ theoretical value of Co_3O_4 was about 4.94 eV, which lower than that of Fe_3O_4 (Fig. S26), in consistent with the results obtained by UPS. The disparity in the previously mentioned Φ values fulfills the conditions necessary for the establishment of interface energy barriers and supports the theoretical feasibility of charge transfer from Co_3O_4 to FeO_x at the p-n heterojunction.

Combining the E_g , E_{VB} and E_{CB} positions, the energy band structures of Co_3O_4 and FeO_x and the corresponding heterojunction are schematically displayed in Fig. 5d. The existence of p-n heterojunction between Co_3O_4 and FeO_x generated a BIEF that enhanced electron interaction between Co_3O_4 and FeO_x . The as-generated BIEF can facilitate electron

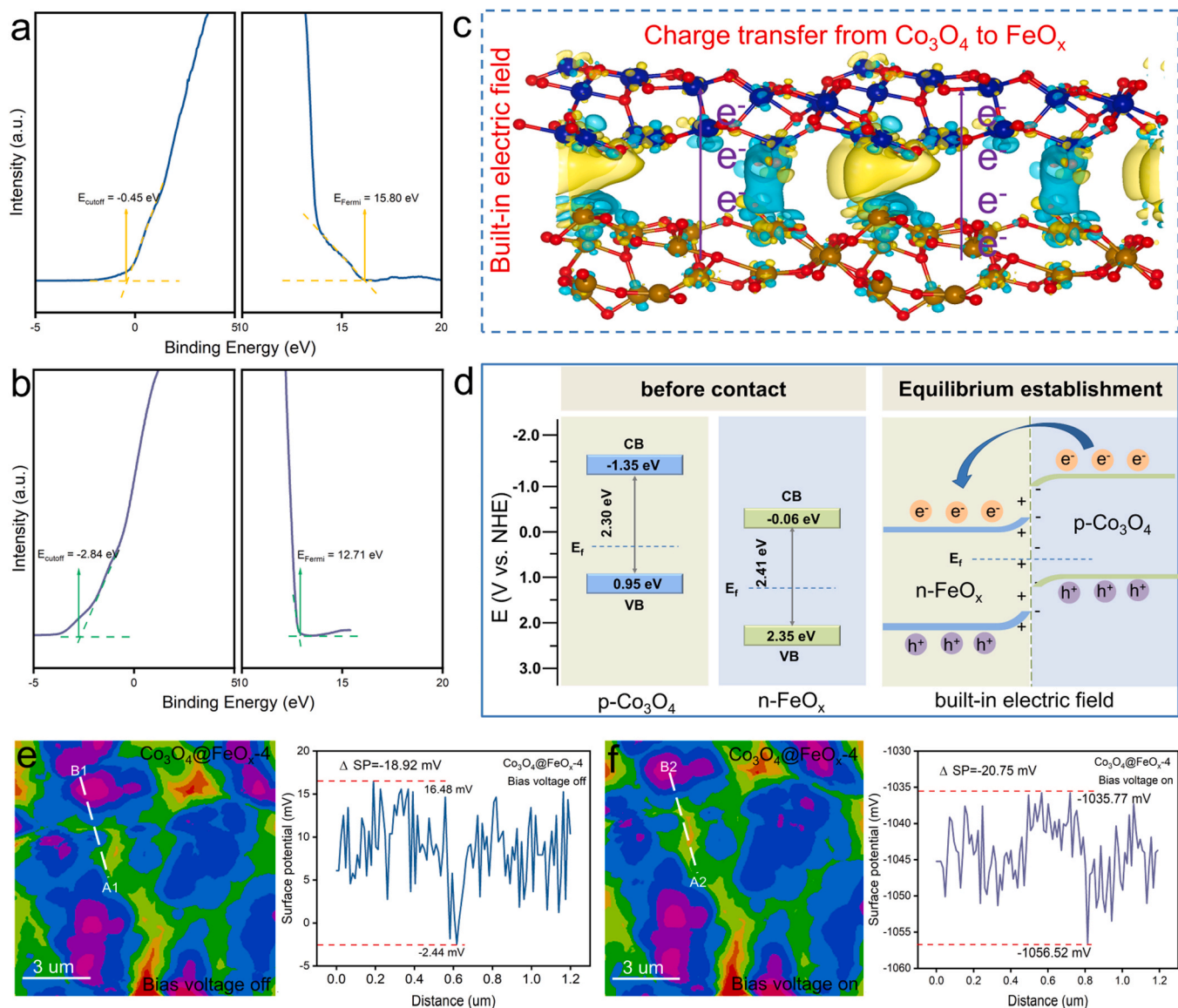


Fig. 5. (a) UPS spectra of the Co_3O_4 ; (b) UPS spectra of the FeO_x ; (c) Simulated differential charge density distribution at the interface between Co_3O_4 and FeO_x , where Co, Fe and O atoms are in brown, blue, and red, respectively; (d) Energy band structure of Co_3O_4 and FeO_x (left), and the schematic of interface electronic structure in the p-n heterojunction (right); (e, f) KPFM potential image under bias voltage off/on for $\text{Co}_3\text{O}_4/\text{FeO}_x-4$ and corresponding surface potential curves, respectively.

transport and improve the conductivity. When Co_3O_4 and FeO_x formed a p-n heterojunction interface, electrons flowed from the Co_3O_4 to FeO_x . Therefore, the $\text{Co}_3\text{O}_4/\text{FeO}_x$ with BIEF can accelerate electron transport, thereby enhancing the limited capture reduction of uranium.

As a dynamic driving force, the BIEF facilitates electron transfer between Co_3O_4 and FeO_x . To deeply verify the electrons transfer behaviors of the BIEF, the three-dimensional (3D) surface potentials of $\text{Co}_3\text{O}_4/\text{FeO}_x-4$ are investigated via in-situ Kelvin Probe Force Microscopy (KPFM) under bias voltage off/on conditions [40,41]. As shown in Fig. 5e and f, the surface potential of $\text{Co}_3\text{O}_4/\text{FeO}_x-4$ at position A2 and B2 were both increased in comparison with position A1 and position B1, indicating that the process of electron transferred was generated with the introduction of voltage. In addition, the interfacial electric field intensity was quantitatively assessed before and after applying voltage by analyzing the differentiation of the fitted surface potential profiles. The surface potential difference (ΔSP) of $\text{Co}_3\text{O}_4/\text{FeO}_x-4$ in bias voltage on was -20.75 mV , which was much higher than that of $\text{Co}_3\text{O}_4/\text{FeO}_x-4$ in bias voltage off (-18.92 mV). The above results strongly confirmed that the $\text{Co}_3\text{O}_4/\text{FeO}_x$ heterojunction established a potent interfacial

electric field between the Co_3O_4 and FeO_x components, thereby bolstering the electro-assisted uranium extraction capabilities of $\text{Co}_3\text{O}_4/\text{FeO}_x$.

Furthermore, to reveal the effect of surface M-O-H coordination bonds on the confined capture of uranyl ions, the XAFS characterization at U $L_{3\text{-edge}}$ is performed on uranium loaded $\text{Co}_3\text{O}_4/\text{FeO}_x-4$. Fig. 6a shows the U $L_{3\text{-edge}}$ X-ray absorption near-edge structure (XANES) spectra, where the distinct peak at approximately $17,166 \text{ eV}$ was the well-known white-line peak, indicating the electron transfer from occupied U 2p to unoccupied 6d states. Accordingly, the absorption edges for uranium-loaded $\text{Co}_3\text{O}_4/\text{FeO}_x-4$ were positioned between those of $\text{UO}_2(\text{NO}_3)_2$, U_3O_8 , and UO_2 , signifying that the valence state of uranium cations was in the range of +4 and +6 [42]. And the high-resolution U 4f spectrum further declared the presence of U(IV) and U(VI) in the uranium-reducing species (Fig. S27). Moreover, the fourier transform extended-XAFS (FT-EXAFS) measurement was verified to the actual local structure of uranium-reactive species in the electrocatalytic reaction [43,44]. As illustrated in Fig. 6b, FT-EXAFS spectra showed two representative peaks at 1.08 \AA and 1.60 \AA , corresponding to the first

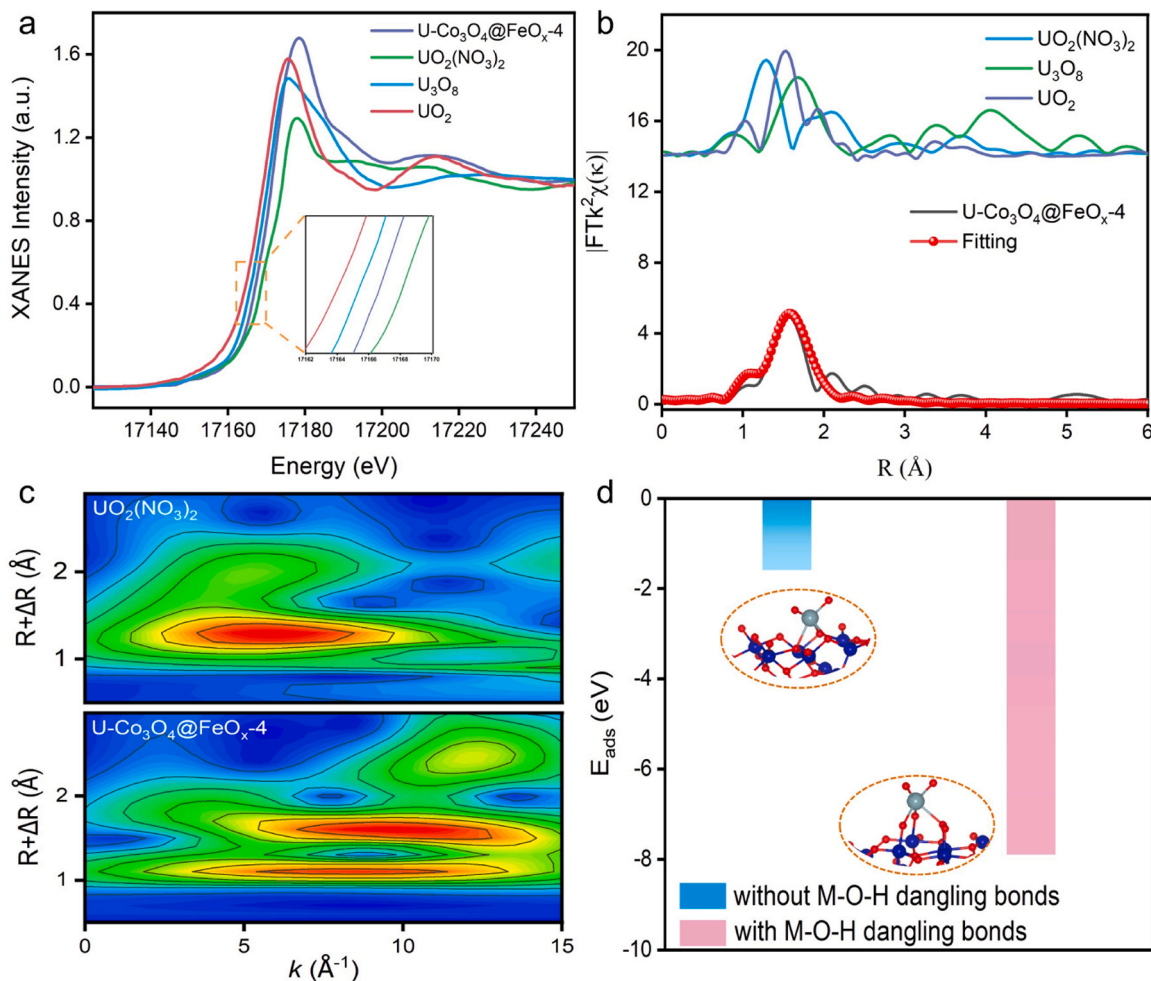


Fig. 6. (a) XANES spectrum showed at the U L_3 -edge of $\text{Co}_3\text{O}_4\text{@FeO}_x\text{-4}$, and the XANES data of the reference standards of $\text{UO}_2(\text{NO}_3)_2$, U_3O_8 and UO_2 ; (b) The corresponding k^2 -weighted FT spectra; (c) WT for $\text{UO}_2(\text{NO}_3)_2$ and $\text{Co}_3\text{O}_4\text{@FeO}_x\text{-4}$; (d) The E_{ads} for $\text{Co}_3\text{O}_4\text{@FeO}_x\text{-4}$ without/with M-O-H coordination bonds, respectively.

U-O shell and the second U-O shell, respectively [45].

Considering the confined capture of uranyl ions by M-O-H coordination bonds, we proceeded to perform a least-squares EXAFS curve fitting analysis, taking into account two backscattering paths involving U-O coordination, which included the first U-O_{ax} shell and the second U-O_{eq} shell. Quantitatively, the corresponding structural parameters of uranium loaded $\text{Co}_3\text{O}_4\text{@FeO}_x\text{-4}$ were summarized in Tab. S3. The best fitting analysis for uranium loaded $\text{Co}_3\text{O}_4\text{@FeO}_x\text{-4}$ gave the coordination numbers (CN) and bond lengths of 1.9 \AA and 1.90 \AA for U-O_{ax} , and 3.1 \AA and 2.28 \AA for U-O_{eq} , respectively [22]. Additionally, to further confirm the structure evolution of uranium-reactive species in the process, wavelet transform (WT) measurement is carried out by the virtue of EXAFS spectra. The WT maximum contour plots of the uranium loaded $\text{Co}_3\text{O}_4\text{@FeO}_x\text{-4}$ changed significantly relative with $\text{UO}_2(\text{NO}_3)_2 \cdot 6\text{H}_2\text{O}$ plots, which strongly supported electrically driven structural evolution of the U-reactive species in the reaction (Fig. 6c). According to the above analysis, we can believe that free uranyl ions were captured by the $\text{Co}_3\text{O}_4\text{@FeO}_x$ to form a sturdy $2\text{O}_{\text{ax}}\text{-1 U-3 O}_{\text{eq}}$ configuration.

Combining with DFT and XAFS, we also studied the effective confinement capture of uranyl ions by M-O-H coordination bonds. Accordingly, we calculated the adsorption energy (E_{ads}) of uranyl ions adsorbed on $\text{Co}_3\text{O}_4\text{@FeO}_x$ without/with M-O-H coordination bonds (Fig. 6d). The E_{ads} of uranyl ions on $\text{Co}_3\text{O}_4\text{@FeO}_x$ with the $2\text{O}_{\text{ax}}\text{-1 U-3 O}_{\text{eq}}$ configuration was calculated to be -7.89 eV , which was considerably lower than that the E_{ads} of uranyl ions on $\text{Co}_3\text{O}_4\text{@FeO}_x$ without M-O-H coordination bonds (-1.58 eV), further showing the presence of

M-O-H coordination bonds enhances the affinity for uranium-reactive species. The above results further confirm that the integration of p-n heterojunction and M-O-H coordination bonds enhances electron transport and promotes confinement capture and reduction of uranium species [46,47].

4. Conclusion

In conclusion, we have designed and fabricated the $\text{Co}_3\text{O}_4\text{@FeO}_x$ nanosheets arrays with supported on the Fe foil for electrochemical extraction of uranium in the fluorine-containing uranium wastewater. Benefiting from self-consistent energy band calculations and in-situ KPFM spectral analysis, we have proven the formation of well-designed BIEF between Co_3O_4 and FeO_x at the p-n heterojunction, offering a strong driving force and transportation highway for accelerating the charge directed migration and promoting electro-assisted uranium extraction. Consequently, the $\text{Co}_3\text{O}_4\text{@FeO}_x$ with p-n heterojunction shows remarkable U(VI) extraction efficiency ($>95\%$) in high fluorine concentrations and over a broad spectrum of uranium concentrations. Utilizing the DFT calculations and XAFS spectra, we distinguish that the $\text{Co}_3\text{O}_4\text{@FeO}_x$ nanosheet arrays improve the adsorption energy for uranium species and form a sturdy $2\text{O}_{\text{ax}}\text{-1 U-3 O}_{\text{eq}}$ configuration, which is achieved by electrically driving the separation of uranium and fluorine. This study paves a valuable guideline for the design and fabrication of the novel and long-lasting $\text{Co}_3\text{O}_4\text{@FeO}_x$ p-n heterojunction with considerable performance, and provides a new research insight for

interface engineering construction.

CRediT authorship contribution statement

Tao Chen: Conceptualization, Formal analysis, Methodology, Project administration, Writing – review & editing. **Wenkun Zhu:** Conceptualization, Formal analysis, Methodology, Writing – review & editing. **Xudong Cui:** Formal analysis, Investigation. **Jie Lian:** Formal analysis, Methodology. **Jin Li:** Data curation, Methodology. **Yi Li:** Conceptualization, Formal analysis, Investigation, Methodology, Writing – review & editing. **Li Zhou:** Conceptualization, Data curation, Formal analysis, Investigation, Methodology, Writing – original draft, Writing – review & editing. **Xi Gong:** Methodology, Data curation. **Qiuyang Li:** Investigation, Methodology. **Gang Wu:** Data curation. **Yuwen Shao:** Data curation, Investigation.

Declaration of Competing Interest

The authors declare that they have no known competing financial interests or personal relationships that could have appeared to influence the work reported in this paper.

Data Availability

Data will be made available on request.

Acknowledgments

This work was supported by the National Natural Science Foundation of China (No. 21976147, U2267224, and 22106126), Sichuan Science and Technology Program (No. 2021YFG0096, 2022YFG0371, and 2023JDRC0068), the Project of State Key Laboratory of Environment-friendly Energy Materials in SWUST (No. 21fksy22), the Research Fund of SWUST for PhD (No. 23zx7103), and the Open Fund of CNNC Key Laboratory for Uranium Extraction from Seawater (KLUES202201). The authors would like to thank Shiyianjia Lab (www.shiyianjia.com) and Suzhou Deyo Bot Advanced Materials Co., Ltd. (www.szdybc.com) for characterization.

Appendix A. Supporting information

Supplementary data associated with this article can be found in the online version at [doi:10.1016/j.apcatb.2024.124052](https://doi.org/10.1016/j.apcatb.2024.124052).

References

- [1] D. Mei, L. Liu, B. Yan, Adsorption of uranium (VI) by metal-organic frameworks and covalent-organic frameworks from water, *Coord. Chem. Rev.* 475 (2023) 214917, <https://doi.org/10.1016/j.ccr.2022.214917>.
- [2] Y. Hu, D. Tang, Z. Shen, L. Yao, G. Zhao, X. Wang, Photochemically triggered self-extraction of uranium from aqueous solution under ambient conditions, *Appl. Catal. B: Environ.* 322 (2023) 122092, <https://doi.org/10.1016/j.apcatb.2022.122092>.
- [3] Z.J. Li, Z.W. Huang, W.L. Guo, L. Wang, L.R. Zheng, Z.F. Chai, W.Q. Shi, Enhanced photocatalytic removal of uranium(VI) from aqueous solution by magnetic TiO₂/Fe₃O₄ and its graphene composite, *Environ. Sci. Technol.* 51 (2017) 5666–5674, <https://doi.org/10.1021/acs.est.6b05313>.
- [4] E. Schneider, B. Carlsen, E. Tavriles, C. van der Hoeven, U. Phathanapirom, Measures of the environmental footprint of the front end of the nuclear fuel cycle, *Energy Econ.* 40 (2013) 898–910, <https://doi.org/10.1016/j.eneco.2013.01.002>.
- [5] Y. Ohashi, S. Murashita, M. Nomura, Extraction of uranium from solid waste containing uranium and fluorine, *Miner. Eng.* 61 (2014) 32–39, <https://doi.org/10.1016/j.mineng.2014.03.003>.
- [6] G. Cifuentes, I. Germain, B. Garrido, M. Cifuentes-Cabezas, P. Orrego, I. Gentico, E. Pino, C. Calderón, Tetra-uranium fluoride electrowinning by electro-electrodialysis cell (EED), *Sep. Purif. Technol.* 281 (2022) 119833, <https://doi.org/10.1016/j.seppur.2021.119833>.
- [7] X. Liu, Y. Xie, M. Hao, Z. Chen, H. Yang, G.I.N. Waterhouse, S. Ma, X. Wang, Highly efficient electrocatalytic uranium extraction from seawater over an amidoxime-functionalized In–N–C catalyst, *Adv. Sci.* 9 (2022) 2201735, <https://doi.org/10.1002/advs.202201735>.
- [8] Y. Ye, B. Fan, Z. Qin, X. Tang, Y. Feng, M. Lv, S. Miao, H. Li, Y. Chen, F. Chen, Y. Wang, Electrochemical removal and recovery of uranium: effects of operation conditions, mechanisms, and implications, *J. Hazard. Mater.* 432 (2022) 128723, <https://doi.org/10.1016/j.jhazmat.2022.128723>.
- [9] D. Wang, J. Zhou, Y. Zhang, J. Zhang, J. Liang, J. Zhang, J. Li, The electrosorption of uranium (VI) onto the modified porous biocarbon with ammonia low-temperature plasma: kinetics and mechanism, *Chem. Eng. J.* 463 (2023) 142413, <https://doi.org/10.1016/j.cej.2023.142413>.
- [10] Y. Wang, Y. Wang, M. Song, S. Chen, J. Wei, J. You, B. Zhou, S. Wang, Electrochemical-mediated regenerable FeII active sites for efficient uranium extraction at ultra-low cell voltage, *Angew. Chem. Int. Ed.* 62 (2023) e202217601, <https://doi.org/10.1002/anie.202217601>.
- [11] X. Tang, Y. Liu, M. Liu, H. Chen, P. Huang, H. Ruan, Y. Zheng, F. Yang, R. He, W. Zhu, Sulfur edge in molybdenum disulfide nanosheets achieves efficient uranium binding and electrocatalytic extraction in seawater, *Nanoscale* 14 (2022) 6285–6290, <https://doi.org/10.1039/D2NR01000C>.
- [12] Y. Liao, R. Lei, X. Weng, C. Yan, J. Fu, G. Wei, C. Zhang, M. Wang, H. Wang, Uranium capture by a layered 2D/2D niobium phosphate/holey graphene architecture via an electro-adsorption and electrocatalytic reduction coupling process, *J. Hazard. Mater.* 442 (2023) 130054, <https://doi.org/10.1016/j.jhazmat.2022.130054>.
- [13] F. Li, M. Du, X. Xiao, Q. Xu, Self-supporting metal-organic framework-based nanoarrays for electrocatalysis, *ACS Nano* 16 (2022) 19913–19939, <https://doi.org/10.1021/acsnano.2c09396>.
- [14] J. Huang, Z. Liu, D. Huang, T. Jin, Y. Qian, Efficient removal of uranium (VI) with a phytic acid-doped polypyrrole/ carbon felt electrode using double potential step technique, *J. Hazard. Mater.* 433 (2022) 128775, <https://doi.org/10.1016/j.jhazmat.2022.128775>.
- [15] J. Huang, Z. Liu, D. Huang, T. Jin, Y. Qian, Electrochemical deposition of uranium oxide with an electrocatalytically active electrode using double potential step technique, *Chin. Chem. Lett.* 33 (2022) 3762–3766, <https://doi.org/10.1016/j.ccllet.2021.11.008>.
- [16] S. Yu, H. Tang, D. Zhang, S. Wang, M. Qiu, G. Song, D. Fu, B. Hu, X. Wang, MXenes as emerging nanomaterials in water purification and environmental remediation, *Sci. Total Environ.* 811 (2022) 152280, <https://doi.org/10.1016/j.scitotenv.2021.152280>.
- [17] X. Zhao, M. Liu, Y. Wang, Y. Xiong, P. Yang, J. Qin, X. Xiong, Y. Lei, Designing a built-in electric field for efficient energy electrocatalysis, *ACS Nano* 16 (2022) 19959–19979, <https://doi.org/10.1021/acsnano.2c09888>.
- [18] Y. Xu, Y. Sheng, M. Wang, T. Ren, K. Shi, Z. Wang, X. Li, L. Wang, H. Wang, Interface coupling induced built-in electric fields boost electrochemical nitrate reduction to ammonia over CuO@MnO₂ core-shell hierarchical nanoarrays, *J. Mater. Chem. A* 10 (2022) 16883–16890, <https://doi.org/10.1039/D2TA02006H>.
- [19] S. Song, S. Zhang, S. Huang, R. Zhang, L. Yin, Y. Hu, T. Wen, L. Zhuang, B. Hu, X. Wang, A novel multi-shelled Fe₃O₄@MnO_x hollow microspheres for immobilizing U(VI) and Eu(III), *Chem. Eng. J.* 355 (2019) 697–709, <https://doi.org/10.1016/j.cej.2018.08.205>.
- [20] N. Li, M. Yin, D.C.W. Tsang, S. Yang, J. Liu, X. Li, G. Song, J. Wang, Mechanisms of U(VI) removal by biochar derived from Ficus microcarpa aerial root: a comparison between raw and modified biochar, *Sci. Total Environ.* 697 (2019) 134115, <https://doi.org/10.1016/j.scitotenv.2019.134115>.
- [21] H. Liu, J. Lei, J. Chen, Y. Li, C. Gong, S. Yang, Y. Zheng, N. Lu, Y. Liu, W. Zhu, R. He, Hydrogen-incorporated vanadium dioxide nanosheets enable efficient uranium confinement and photoreduction, *Nano Res.* 15 (2022) 2943–2951, <https://doi.org/10.1007/s12274-021-3916-8>.
- [22] L. Zhou, J. Lian, Q. Li, J. Li, Y. Shao, G. Wu, T. Ding, X. Cui, T. Chen, W. Zhu, Unveiling the critical role of surface hydroxyl groups for electro-assisted uranium extraction from wastewater, *Inorg. Chem.* 62 (2023) 21518–21527, <https://doi.org/10.1021/acs.inorgchem.3c03967>.
- [23] S. Fu, Y. Ma, X. Yang, X. Yao, Z. Jiao, L. Cheng, P. Zhao, Defect and interface engineering of hexagonal Fe₂O₃/ZnCo₂O₄ n-n heterojunction for efficient oxygen evolution reaction, *Appl. Catal. B: Environ.* 333 (2023) 122813, <https://doi.org/10.1016/j.apcatb.2023.122813>.
- [24] P. Gao, Y. Zeng, P. Tang, Z. Wang, J. Yang, A. Hu, J. Liu, Understanding the synergistic effects and structural evolution of Co(OH)₂ and Co₃O₄ toward boosting electrochemical charge storage, *Adv. Funct. Mater.* 32 (2022) 2108644, <https://doi.org/10.1002/adfm.202108644>.
- [25] X. Chen, B. Liu, C. Zhong, Z. Liu, J. Liu, L. Ma, Y. Deng, X. Han, T. Wu, W. Hu, J. Lu, Ultrathin Co₃O₄ layers with large contact area on carbon fibers as high-performance electrode for flexible zinc-air battery integrated with flexible display, *Adv. Energy Mater.* 7 (2017) 1700779, <https://doi.org/10.1002/aenm.201700779>.
- [26] G. Mu, Y. Zeng, Y. Zheng, Y. Cao, F. Liu, S. Liang, Y. Zhan, L. Jiang, Oxygen vacancy defects engineering on Cu-doped Co₃O₄ for promoting effective COS hydrolysis, *Green. Energy Environ.* 8 (2023) 831–841, <https://doi.org/10.1016/j.gee.2021.11.001>.
- [27] X. Yan, G. Li, K. Shen, C. Wang, K. Wang, Electrochemically grown Fe₂O₃/Fe₃O₄ heterostructure nanotubes with In₂O₃ induced tandem internal electric fields for enhanced photoelectrochemical water oxidation, *Green. Chem.* 25 (2023) 9394–9404, <https://doi.org/10.1039/D3GC03466F>.
- [28] J. Li, Z. Cui, Y. Zheng, X. Liu, Z. Li, H. Jiang, S. Zhu, Y. Zhang, P.K. Chu, S. Wu, Atomic-layer Fe₂O₃-modified 2D porphyrinic metal-organic framework for enhanced photocatalytic disinfection through electron-withdrawing effect, *Appl. Catal. B: Environ.* 317 (2022) 121701, <https://doi.org/10.1016/j.apcatb.2022.121701>.

- [29] Q. Yan, X. Li, Q. Zhao, G. Chen, Shape-controlled fabrication of the porous Co_3O_4 nanoflower clusters for efficient catalytic oxidation of gaseous toluene, *J. Hazard. Mater.* 209–210 (2012) 385–391, <https://doi.org/10.1016/j.jhazmat.2012.01.039>.
- [30] X. Liang, X. Wang, M. Yang, H. Dong, Y. Ji, L. Wang, J. Zhang, C. Long, $\alpha\text{-Fe}_2\text{O}_3$ -supported Co_3O_4 nanoparticles to construct highly active interfacial oxygen vacancies for ozone decomposition, *Environ. Pollut.* 330 (2023) 121704, <https://doi.org/10.1016/j.envpol.2023.121704>.
- [31] X. Wang, Y. Zhou, J. Luo, F. Sun, J. Zhang, Synthesis of V-doped urchin-like NiCo_2O_4 with rich oxygen vacancies for electrocatalytic oxygen evolution reactions, *Electrochim. Acta* 406 (2022) 139800, <https://doi.org/10.1016/j.electacta.2021.139800>.
- [32] K. Zhang, G. Zhang, J. Qu, H. Liu, Disorder the atomic structure of Co(II) oxide via B-doping: an efficient oxygen vacancy introduction approach for high oxygen evolution reaction electrocatalysts, *Small* 14 (2018) 1802760, <https://doi.org/10.1002/smll.201802760>.
- [33] P. Wang, X. Liu, W. Qiu, F. Wang, H. Jiang, M. Chen, W. Zhang, J. Ma, Catalytic degradation of micropollutant by peroxymonosulfate activation through Fe(III)/Fe(II) cycle confined in the nanoscale interlayer of Fe(III) -saturated montmorillonite, *Water Res.* 182 (2020) 116030, <https://doi.org/10.1016/j.watres.2020.116030>.
- [34] Y. Wang, M. Song, J. Wei, J. You, S. Chen, S. Wang, Y. Wang, Strengthening Fe(II)/Fe(III) dynamic cycling by surface sulfation to achieve efficient electrochemical uranium extraction at ultralow cell voltage, *Environ. Sci. Technol.* 57 (2023) 13258–13266, <https://doi.org/10.1021/acs.est.3c05133>.
- [35] L. Wang, G. Tang, S. Liu, H. Dong, Q. Liu, J. Sun, H. Tang, Interfacial active-site-rich $0\text{D } \text{Co}_3\text{O}_4/1\text{D } \text{TiO}_2$ p-n heterojunction for enhanced photocatalytic hydrogen evolution, *Chem. Eng. J.* 428 (2022) 131338, <https://doi.org/10.1016/j.cej.2021.131338>.
- [36] Y. Teng, J.H. Chen, Y.H. Huang, Z.C. Zhou, X.D. Wang, D.B. Kuang, H.Y. Chen, Atom-triggered epitaxial growth of Bi-based perovskite heterojunctions for promoting interfacial charge transfer, *Appl. Catal. B: Environ.* 335 (2023) 122889, <https://doi.org/10.1016/j.apcatb.2023.122889>.
- [37] Y. Yang, S. Zhao, F. Bi, J. Chen, Y. Wang, L. Cui, J. Xu, X. Zhang, Highly efficient photothermal catalysis of toluene over $\text{Co}_3\text{O}_4/\text{TiO}_2$ p-n heterojunction: the crucial roles of interface defects and band structure, *Appl. Catal. B: Environ.* 315 (2022) 121550, <https://doi.org/10.1016/j.apcatb.2022.121550>.
- [38] H. Li, C. Chen, Y. Yan, T. Yan, C. Cheng, D. Sun, L. Zhang, Utilizing the built-in electric field of p-n junctions to spatially propel the stepwise polysulfide conversion in lithium-sulfur batteries, *Adv. Mater.* 33 (2021) 2105067, <https://doi.org/10.1002/adma.202105067>.
- [39] X. Zou, Y. Dong, J. Ke, H. Ge, D. Chen, H. Sun, Y. Cui, Cobalt monoxide/tungsten trioxide p-n heterojunction boosting charge separation for efficient visible-light-driven gaseous toluene degradation, *Chem. Eng. J.* 400 (2020) 125919, <https://doi.org/10.1016/j.cej.2020.125919>.
- [40] J. Wan, L. Liu, Y. Wu, J. Song, J. Liu, R. Song, J. Low, X. Chen, J. Wang, F. Fu, Y. Xiong, Exploring the polarization photocatalysis of ZnIn_2S_4 material toward hydrogen evolution by integrating cascade electric fields with hole transfer vehicle, *Adv. Funct. Mater.* 32 (2022) 2203252, <https://doi.org/10.1002/adfm.202203252>.
- [41] B. Tu, K. Yu, D. Fu, L. Zhou, R. Wang, X. Jiang, H. Liu, X. Cao, X. Gong, R. He, Y. Tang, T. Chen, W. Zhu, Amino-rich $\text{Ag-NWs/NH}_2\text{-MIL-125(Ti)}$ hybrid heterostructure via LSPR effect for photo-assist uranium extraction from fluorine-containing uranium wastewater without sacrificial agents, *Appl. Catal. B: Environ.* 337 (2023) 122965, <https://doi.org/10.1016/j.apcatb.2023.122965>.
- [42] T. Chen, P. He, T. Liu, L. Zhou, M. Li, K. Yu, Q. Meng, J. Lian, W. Zhu, MXene-derived 3D defect-rich TiO_2 @Reduced graphene oxide aerogel with ultrafast carrier separation for photo-assisted uranium extraction: a combined batch, x-ray absorption spectroscopy, and density functional theory calculations, *Inorg. Chem.* 61 (2022) 12759–12771, <https://doi.org/10.1021/acs.inorgchem.2c01850>.
- [43] H. Yang, X. Liu, M. Hao, Y. Xie, X. Wang, H. Tian, G.I.N. Waterhouse, P.E. Kruger, S.G. Telfer, S. Ma, Functionalized iron-nitrogen-carbon electrocatalyst provides a reversible electron transfer platform for efficient uranium extraction from seawater, *Adv. Mater.* 33 (2021) 2106621, <https://doi.org/10.1002/adma.202106621>.
- [44] Y. Ye, J. Jin, W. Han, S. Miao, Y. Feng, Z. Qin, X. Tang, C. Li, Y. Chen, F. Chen, Y. Wang, Spontaneous electrochemical uranium extraction from wastewater with net electrical energy production, *Nat. Water* 1 (2023) 887–898, <https://doi.org/10.1038/s44221-023-00134-0>.
- [45] T. Chen, T. Liu, L. Zhou, M. Li, Q. Meng, K. Yu, J. Lian, W. Zhu, Ternary boron carbon nitrides hollow nanotubes with tunable p-n homojunction for photo-assisted uranium extraction: a combined batch, EXAFS and DFT calculations, *Appl. Catal. B: Environ.* 318 (2022) 121815, <https://doi.org/10.1016/j.apcatb.2022.121815>.
- [46] M. Li, R. Wang, T. Liu, Q. Chen, N. Li, L. Zhou, K. Yu, H. Liu, X. Gong, R. He, F. Ahmad, F. Yang, W. Zhu, T. Chen, Integrating surface functional modification and energy-level adapted coupling of photocatalyst with ultrafast carrier separation for uranium extraction, *Sep. Purif. Technol.* 309 (2023) 123121, <https://doi.org/10.1016/j.seppur.2023.123121>.
- [47] J. Wei, S. Chen, Y. Jiang, Z. Liu, Y. Wang, J. You, F. Zhang, Y. Cao, S. Wang, Y. Wang, Selective anchoring by surface sulfur species coupled with rapid interface electron transfer for ultrahigh capacity extraction of uranium from seawater, *Environ. Sci. Technol.* 57 (2023) 21908–21916, <https://doi.org/10.1021/acs.est.3c07719>.